JAAS

PAPER

View Article Online
View Journal | View Issue

Open Access Article. Published on 06 February 2026. Downloaded on 4/18/2026 5:39:06 PM.
This article is licensed under a Creative Commons Attribution 3.0 Unported Licence.

Check for updates

Cite this: *J. Anal. At. Spectrom.*, 2026, **41**, 1048

Received 26th September 2025
Accepted 5th January 2026

DOI: 10.1039/d5ja00374a

rsc.li/jaas

Quantification of spacecraft heatshield contaminants seen in reentry shock layer emissions using calibration-free LIBS

Keira J. Leistikow,[a] Noshin Nawar, [b] Justin I. Borrero-Negrón, [c]
Marat Kulakhmetov,[d] Paolo Valentini [b] and Ashwin P. Rao [*b]

Shock layer thermochemistry during atmospheric reentry of spacecraft is strongly influenced by the composition of thermal protection system (TPS) materials. In this study, we implement calibration-free laser-induced breakdown spectroscopy (CF-LIBS) to profile cross-sections of phenolic impregnated carbon ablator (PICA) and room temperature vulcanizing (RTV) silicone from the heatshield of a commercial reentry capsule. CF-LIBS measurements determine that these materials contain alkali and alkaline earth contaminants (*e.g.*, Na, Ca) at levels up to 10 parts-per-million (ppm) and heavier metals like Fe at 10^3 ppm. Contaminant concentrations are linked to observed strong atomic radiators identified from *in situ* shock layer emissions taken during reentry, demonstrating the value of CF-LIBS for interpreting complex shock-layer emission data from reentry spacecraft.

1 Introduction

Spacecraft thermal protection systems (TPS) must withstand extreme aerothermodynamic conditions during atmospheric reentry. The bow shocks ahead of reentry bodies heat the surrounding air to temperatures in excess of 15 000 K and create high-enthalpy flowfields with thermochemical nonequilibrium.[1,2] The combined radiative and convective heating from these flowfields can exceed 1 kW cm^{-2} on the surface of the spacecraft.[3] Ablative TPS, such as phenolic impregnated carbon ablator (PICA), mitigate this thermal loading by absorbing thermal energy through endothermic processes, which decompose the heatshield into high temperature volatile species.[4] These gaseous products pass through the TPS into the shock layer, dissipating heat from the spacecraft surface into the surrounding air flow. These molecules undergo further complex chemical interactions with shock-heated air species, influencing the evolution of shock layer chemistry and radiative emissions during reentry.[5,6]

Varda Space Industries, an American space manufacturing startup, has developed a ballistic reentry capsule to enable commercial orbital manufacturing needs and serve as a standard hypersonic testbed for the research community. The testbed helps develop advanced heat shields, flight sensors, and communication systems, while providing an avenue for data collection to advance state-of-the-art modeling of hypersonic flows. On the 28th of February 2025, the Varda's W-2 capsule successfully executed an orbital reentry flight test into Koonibba Test Range, South Australia. W-2 housed an optical emission spectroscopy (OES) payload developed by the U.S. Air Force Research Laboratory called: Optical Sensing of Plasmas in the ReEntry Environment (OSPREE).[7,8] The OSPREE payload captured Vis-NIR (340–800 nm) *in situ* spectral emission data of the reentry shock layer at speeds in excess of Mach 25, providing critical data needed for the development and validation of *ab initio* hypersonic air chemistry models.[9] Interestingly, OSPREE detected strongly radiating atomic emissions of metallic elements such as Na and Fe in the reentry shock layer, which were not expected from the predicted heatshield ablation chemistry. The capsule forebody TPS chars and pyrolyzes in flight, injecting material from the heatshield into the flowfield. Thus, it became important to characterize the constituents of the capsule TPS to aid post-flight data analysis and support designs of future flight experiments on the Varda testbed.

Chemical makeup of the Varda capsule forebody heatshield is analyzed using laser-induced breakdown spectroscopy (LIBS). LIBS has emerged as a powerful method for *in situ* material characterization, requiring little to no sample preparation and providing rapid, efficient, and sensitive field analyses.[10,11] Focusing a pulsed laser with moderate to high irradiance levels (~GW cm^{-2}) onto the surface of a target ablates the sample surface, and generates a laser-produced plasma (LPP). In this technique, the LPP typically exhibits extreme temperatures greater than 10^3 K and less than 10^5 K and high electron densities greater than 10^{20} m^{-3} up to approximately 10^{25} m^{-3} over a broad timescale relative to the laser pulse duration (*e.g.*,

---

[a] University of California San Diego, La Jolla, CA, USA

[b] Space Vehicles Directorate, Air Force Research Laboratory, Kirtland Air Force Base, NM, USA. E-mail: ashwin.rao.1@spaceforce.mil

[c] Nuclear Engineering Program, University of Florida, Gainesville, FL, USA

[d] Varda Space Industries, El Segundo, CA, USA

This journal is © The Royal Society of Chemistry 2026

Open Access Article. Published on 06 February 2026. Downloaded on 4/18/2026 5:39:06 PM.
This article is licensed under a Creative Commons Attribution 3.0 Unported Licence.

ns-, ps-, or fs-pulsed laser).[12] The resultant luminescent plasma is composed of excited atoms and molecules, which produce optical emission signatures at specific wavelengths characteristic of the target's elemental composition, making LIBS a viable method to analyze chemical composition of various materials. In prior literature, LIBS has proven to be a versatile chemical analysis tool with applications in geochemistry,[13,14] nuclear science,[15–19] metallurgy,[20] and environmental science.[21,22] LIBS has also been used to study chemical kinetics of high-temperature materials, such as carbon composites, in plasma environments.[23]

A method called calibration-free LIBS (CF-LIBS) was introduced by Ciucci *et al.*[24] to overcome the limitations of LIBS due to quantitative uncertainties arising from emission signal dependencies on the sample matrix in which an element is embedded, or "matrix effects". CF-LIBS removes the need to perform measurements of a standard sample set and relate changes in LIBS spectral emission intensity to known changes in analyte quantity. Instead, CF-LIBS proposes using analytical equations with measured line intensities and tabulated transition parameters to determine elemental concentrations from measured spectra.[25] CF-LIBS has been widely reported as a useful analytical method across a wide range of materials.[26–30] Detection limits below the single part-per-million have been reported, although limit of detection in CF-LIBS appears to vary between studies due to dependent on experimental parameters such as laser-produced plasma emitter densities and plasma temperature.[31–33] Nevertheless, CF-LIBS presents a promising avenue for investigating elemental contaminants in spacecraft heatshields where a calibration standard sample set is not available.

We present the implementation of CF-LIBS to identify and quantify metallic elemental contaminants in materials comprising the forebody heatshield of the W-2 reentry capsule. The identified spectral emissions and calculated concentrations of these elements are compared directly to OES data obtained during atmospheric reentry. The laboratory measurements are used to explain the source of these metallic emissions seen in shock layer OES data. The aerodynamics of the vehicle and gas–surface interactions during reentry are discussed to explain the physical mechanisms introducing these metals into the reentry plasma and their effects on shock layer thermochemistry.

2 *In situ* OES observations during atmospheric reentry

The OSPREE OES payload used an Ocean Optics HR2 spectrometer to obtain Vis-NIR (340–800 nm) *in situ* spectra of the shock layer during an atmospheric reentry mission. Optical emissions were obtained from a line of sight (LOS) on the shoulder of the vehicle through an optical window on the capsule backshell. Fig. 1 provides a fluid dynamics solution contour plot of the vehicle showing the exact LOS geometry from the vehicle aft dome into the shock layer. Full details of the design of the payload and mission can be found in Rao *et al.* (2025),[7] while comprehensive results of the mission including

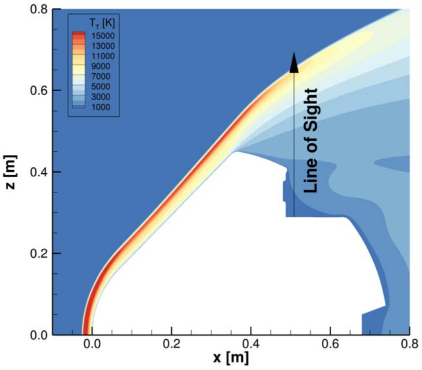

Fig. 1 Flowfield translational temperature contour plot of W-2 cross section with annotated optical line of sight into the shock layer used for emission collection.

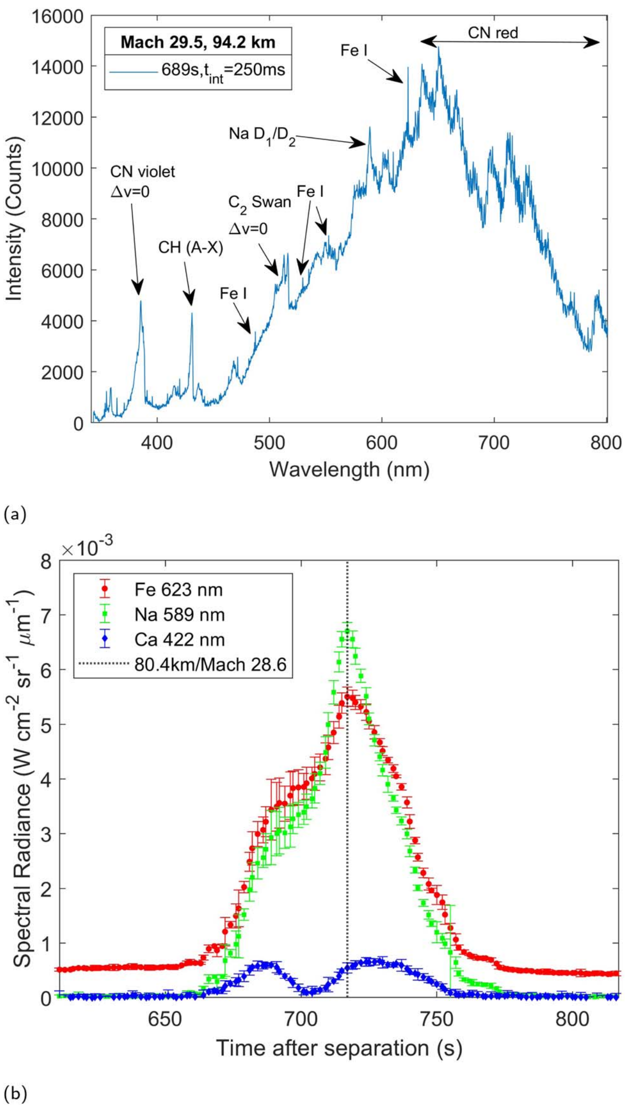

Fig. 2 Flight data from the OSPREE reentry experiment showing (a) raw spectrum of shock layer radiance at 94 km with Na and Fe atomic emissions and (b) spectral radiance of Fe, Na, and Ca observed during flight. The data prior to 660 s in flight is effectively noise recorded by the spectrometer in the presence of a non-radiating shock layer.

Open Access Article. Published on 06 February 2026. Downloaded on 4/18/2026 5:39:06 PM. This article is licensed under a Creative Commons Attribution 3.0 Unported Licence.

a full analysis of collected OES data can be read in ref. 34. Fig. 2(a) shows a raw spectrum taken during flight at 94.2 km.

The spectrum exhibits many molecular emission features (CN, CH, C_2) resulting from breakdown and interaction of PICA pyrolysis products with the surrounding shock heated air, as well as two strong atomic emissions at 589 nm and 623.3 nm identified as neutral Na and Fe, respectively. Multiple smaller emissions of Fe I are seen at 487.3 nm, 529.5 nm, and 552.6 nm. Further investigation of weaker emissions in the data set revealed the presence of the Ca I emission at 422.6 nm. The presence of strong atomic emissions of alkali, alkaline earth, and other metallic species in the flight data was unexpected, and analysis of the measured spectral radiance over time indicated continuous injection of these elemental contaminants into the shock layer during flight. Fig. 2(b) shows the spectral radiance of Fe I (623.3 nm), Na I (589 nm), and Ca I (422.6 nm) from 620–810 s into reentry. This data reflects strong spectral radiance from Fe and Na peaking around 80 km, with minor contributions from Ca throughout reentry. Based on the time-evolving radiance trends, it was hypothesized that these atomic emissions stem from contaminants in the vehicle forebody heatshield which are introduced into the shock layer through the various chemical processes accompanying pyrolysis, ablation, and heatshield decomposition during flight.

The presence of metallic impurities in the vehicle TPS has significant effects on shock layer chemistry and radiative heating experienced by the capsule during reentry. Alkali and alkaline earth metals, such as Na, are readily ionized and exhibit large electron-impact cross sections.[35] Bortner 1964 is one of the sole reports detailing the effects of Na on hypervelocity flow chemistry.[36] Two representative reactions for Na impact ionization and Na/NO charge exchange are shown below.

$$\mathrm{Na} + \mathrm{e}^- \rightarrow \mathrm{Na}^+ + \mathrm{e}^- + \mathrm{e}^-$$

$$\mathrm{NO}^+ + \mathrm{Na} \rightarrow \mathrm{NO} + \mathrm{Na}^+$$

The presence of Na in hypervelocity flows can increase shock layer electron density as a result of such reactions.[36,37] Augmented electron density values during reentry have major implications on radiofrequency communications. Because the plasma cutoff frequency is directly related to electron density, electromagnetic waves below the plasma frequency attempting to penetrate a plasma layer will be attenuated.[38] Thus, contributions of alkali metals to shock layer chemistry can have non-trivial second order effects. Na is easily excitable due to its electronic structure, and the D_1/D_2 doublet presents as a strong radiator even when Na is only present in trace quantities.[39] This feature was observed in *ex situ* spectral observations of the Stardust[40] and Hayabusa2 (ref. 41) reentries. Transition metals such as Fe also present as strong radiators due to their dense line emission across the UV-Vis-NIR. Lewis *et al.* observed this in graphite ablation experiments in the X-2 expansion tunnel, noting that Fe contamination in measured emission spectra contributed between 20–40% of the total radiance in the short-wavelength visible band.[42,43] Because radiative emission strength is directly related to incident radiative heat flux on the surface, the presence of strong radiators in the shock layer can increase the radiative heat load experienced during reentry, and their effects must be accounted for in vehicle design. The appearance of these emissions in the OSPREE flight data has sparked great interest in characterizing the W-2 forebody TPS to fully assess the sources of these metallic species and quantify their presence in the heatshield.

3 Experimental methodology

3.1 Materials

In this study, pristine samples of two TPS materials used on the W-2 forebody were investigated: PICA and RTV silicone. This was done to best mimic the state of the heatshield immediately prior to reentry and understand the true native concentrations of metallic impurities in a newly assembled vehicle. PICA is a legacy NASA material created by impregnating a carbon fiber preform with phenolic resole resin.[44] With its low density and high ablative performance, PICA and its variants have been used in several planetary entry vehicles that include: Stardust, Mars Science Laboratory, OSIRIS-REx, Dragon, and Dragonfly.[45,46] The W-series capsule forebodies are assembled in tiled sections rather than as a monolithic shell. A high temperature RTV silicone is used as a gap-filler between PICA tile seams. Fig. 3(a) and (b) show the cross sections of the PICA and RTV samples investigated in this study. The particular PICA sample analyzed in this experiment contains a waterproof coating, roughly 12 mm in depth, to mitigate moisture absorption.

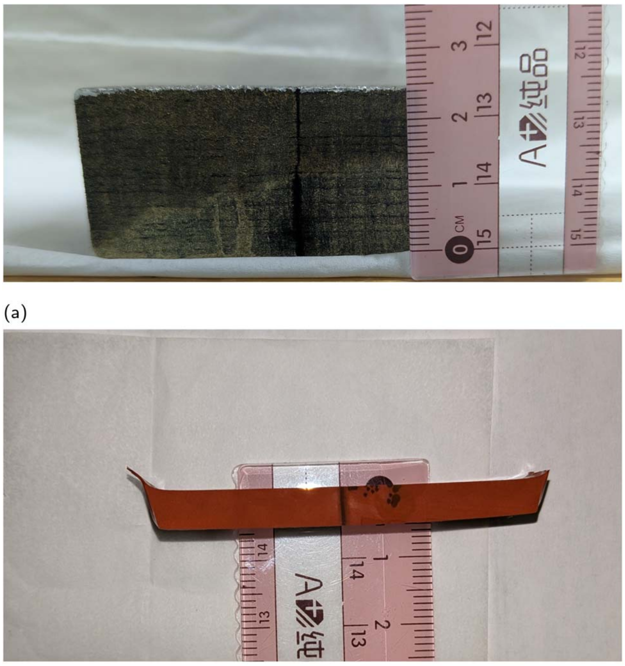
(a)
(b)

Fig. 3 Cross sections of samples of (a) PICA and (b) RTV silicone investigated in this experiment.

Open Access Article. Published on 06 February 2026. Downloaded on 4/18/2026 5:39:06 PM.
This article is licensed under a Creative Commons Attribution 3.0 Unported Licence.

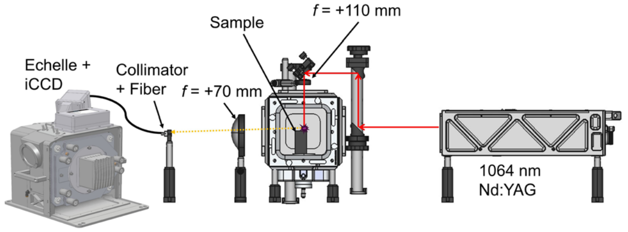

Fig. 4 Diagram of LIBS measurement setup implemented to obtain cross-sectional profile measurements of TPS samples.

3.2 CF-LIBS setup

The experimental setup, shown in Fig. 4, used a New Wave GEMINI 1064 nm Nd:YAG laser with a pulse width of 10 ns and an energy output of 80 mJ per pulse at a repetition rate of 10 Hz to induce breakdown in and ablate the PICA and RTV samples. The 5 mm diameter beam is focused into a 6 × 6 × 6 in. vacuum cube with a plano-convex lens with $f = +110$ mm, yielding a 30 µm spot size on the sample. This process was performed under vacuum at a pressure of 80 mTorr to decrease the presence of molecular emissions (*e.g.*, CN, C_2) resulting from reactions between air molecules and atomic constituents of the samples produced from ablation. Furthermore, conducting LIBS at lower pressure or vacuum conditions has been shown to reduce or eliminate the effects of self-absorption, improving quantitative accuracy.[47–50] LIBS emissions were captured using a secondary lens with $f = +70$ mm and a 74-VIS Ocean Optics collimator. An Echelle spectrograph (Catalina Scientific OWL 325/65) with an ICCD camera (Raptor Photonics Condor) set to 1 ms exposure time, 10 µs gate width, 250 ns gate delay, and MCP gain of 1500 were used for spectral emission capture from 200 nm to 800 nm with $\Delta\lambda = 0.01$ nm. It is standard to use a larger gate width in minor element CF-LIBS quantification to improve signal-to-noise ratio and thus better resolve weak emissions.[51] A digital delay generator (DDG) synchronized the triggering of the ICCD with each laser pulse. An automatic background subtraction was performed in the camera software with the acquisition of each spectrum. A 1-D raster of the ablation point through the length of the sample cross section was conducted using a tri-axis translation stage plate made for the vacuum cube. The micrometer dial was turned to shift the measurement point 0.159 mm per step. 1570 spectra were collected from the PICA sample with 10 shots taken at 157 total locations through the cross section. 320 spectra were collected from the RTV sample with 10 shots taken at 32 total locations. Each set of 10 shots were averaged at every location of the depth profile of both samples, as is standard when using LIBS for quantification of minor elements.[51]

4 Spectral line identification

Fig. 5–8 show the collection of averaged spectra from each location on the PICA sample and Fig. 9–11 show the averaged RTV spectra broken up into various wavelength ranges, highlighting the distinct spectral features observed in each sample.

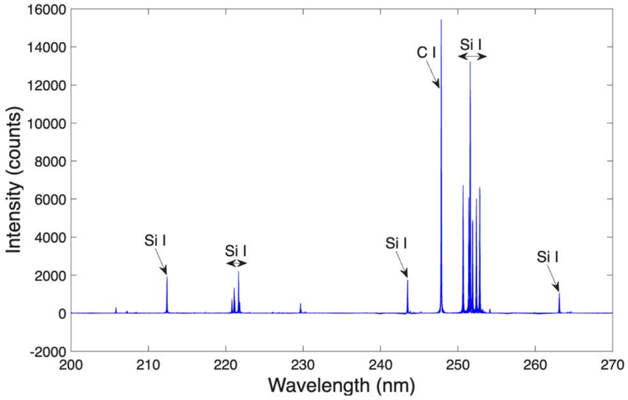

Fig. 5 PICA spectra from 200–270 nm.

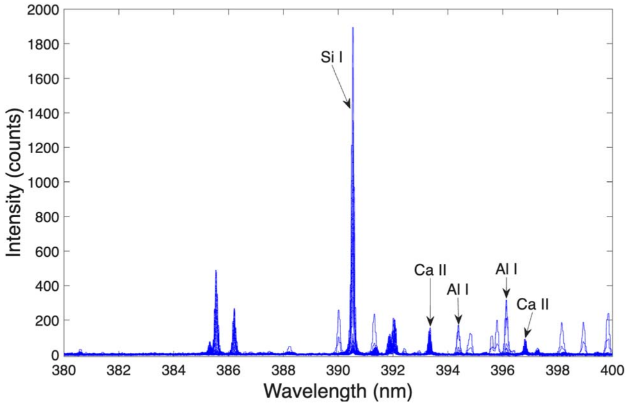

Fig. 6 PICA spectra from 380–400 nm.

Atomic emission lines were identified using data tabulated in the NIST Atomic Spectral Database.[39]

The PICA spectrum is characterized by several Si I emissions, along with C I, Ca II, and Al I lines in the UV (Fig. 5 and 6). Further into the Vis-NIR, H_α (656 nm), the Na D_1/D_2 doublet (588/589 nm), Si II, and O I at 777 nm are observed (Fig. 7 and 8). The presence of C, H, and O emissions stem from the atomic constituents of the phenolic resin. Si, Na, Ca, and Al are not

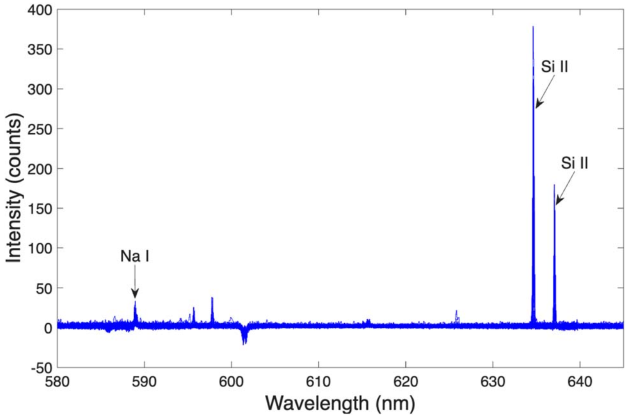

Fig. 7 PICA spectra from 580–645 nm.

Open Access Article. Published on 06 February 2026. Downloaded on 4/18/2026 5:39:06 PM.
This article is licensed under a Creative Commons Attribution 3.0 Unported Licence.

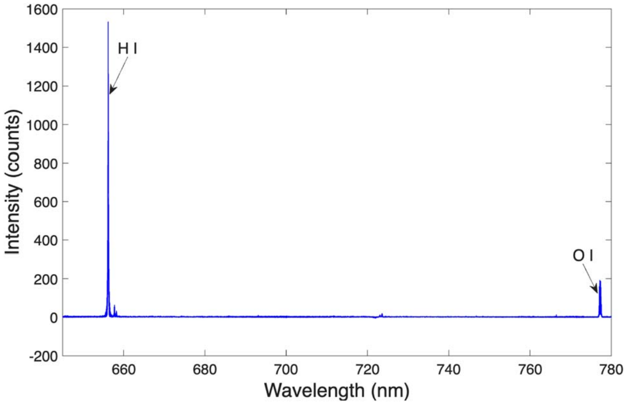

Fig. 8 PICA spectra from 645–780 nm.

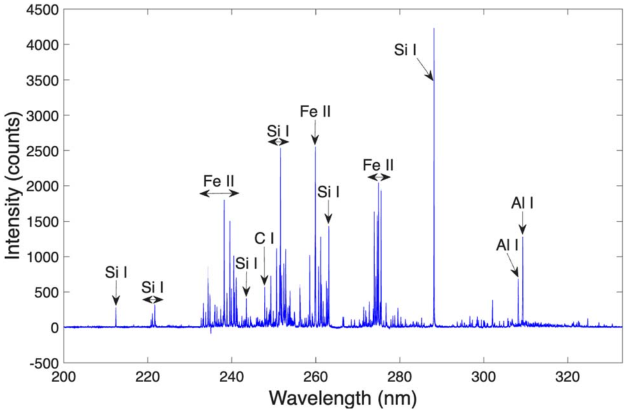

Fig. 9 RTV spectra from 200–333 nm.

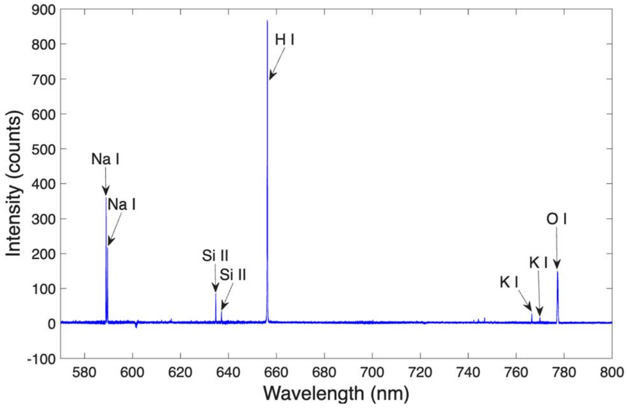

Fig. 11 RTV spectra from 580–800 nm.

Table 1 Key atomic emissions identified in samples with corresponding transition parameters from NIST

Species	λ (nm)	g_kA_{ki} (s^{-1})	E_i (eV)	E_k (eV)	Sample
Si I	288.14	6.51×10^8	0.7810	5.0823	PICA, RTV
Si II	634.68	2.34×10^8	8.1210	10.0739	RTV
Na I	588.96	2.46×10^8	0.0000	2.1044	PICA, RTV
Ca I	422.67	6.54×10^8	0.0000	2.9325	PICA, RTV
Ca II	393.36	5.88×10^8	0.0000	3.1509	PICA, RTV
Al I	396.14	1.97×10^8	0.0139	3.1427	PICA, RTV
C I	247.85	8.40×10^7	2.6840	7.6848	PICA, RTV
H I	656.19	7.93×10^8	10.1988	12.0875	PICA, RTV
O I	777.20	2.58×10^8	9.1461	10.7409	PICA, RTV
Fe I	404.55	7.76×10^8	1.4849	4.5485	RTV
Fe II	259.93	2.35×10^9	0.0000	4.7683	RTV
K I	766.48	1.51×10^8	0.0000	1.6171	RTV

expected in PICA, and were thus labeled as elemental impurities.

In the RTV spectra, Si I, C I, Ca II, and Al I emission lines are identified in the UV along with several Fe I and Fe II emissions (Fig. 9 and 10). In the visible range, the RTV spectra exhibit Na I and Si II lines along with H_α (Fig. 11). K I and O I emissions lines are also seen in the NIR (Fig. 11). The molecular structure of RTV silicone accounts for the presence of Si, C, O, and H, while iron oxide additives are included in the RTV for high-temperature applications account for the presence of Fe. Thus, elemental contaminants found within the RTV are identified as Ca, Al, Na, and K. The spectral line identification of the LIBS data yields insight into the unexpected presence of several strong radiative emission lines observed in the shock layer OES data obtained by OSPREE, indicating that these elements are introduced into the flowfield by the TPS. Since OSPREE's spectral bandwidth did not extend into the UV, the numerous Si emissions seen in the LIBS data were not observed in flight. Al and K were not directly observed during reentry, as emissions from these elements were likely occluded by nearby molecular emission bands from N_2 and O_2. Thus, the initial elemental identification indicates that the Fe, Na, and Ca see in the flight OES data from W-2 stem from constituents of the capsule TPS. Table 1 summarizes the main species emissions identified in the LIBS spectra selected for CF-LIBS analysis.

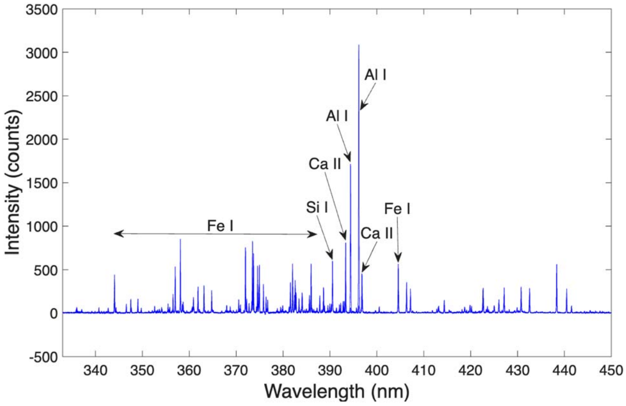

Fig. 10 RTV spectra from 333–450 nm.

5 CF-LIBS analysis and results

5.1 Establishing pLTE conditions

In LIBS, the use of quantitative analysis methodologies dependent on Boltzmann statistics is valid if the LPP is determined to be in partial local thermodynamic equilibrium (pLTE). The

Open Access Article. Published on 06 February 2026. Downloaded on 4/18/2026 5:39:06 PM.
This article is licensed under a Creative Commons Attribution 3.0 Unported Licence.

criterion shown in eqn (1), developed by Fujimoto and McWhirter,[52] is implemented to determine if pLTE conditions are met.

$$n_e > 1.6 \times 10^{12}\sqrt{T}(\Delta E_{ki})^3\ [\mathrm{cm}^{-3}] \tag{1}$$

In this relation, T refers to the plasma temperature (K) and ΔE_{ki} represents the maximum energy difference between the two consecutive excited states (eV) of the spectral lines used. If the electron density (n_e) exceeds the right-hand side (RHS) of the equation then the LPP meets the pLTE criterion. Plasma temperature is determined using the Boltzmann method per eqn (2),

$$\ln\left(\frac{I_\lambda^{ki}\lambda}{g_k A_{ki}}\right) = \frac{-E_k}{k_b T} + \ln\left(\frac{hcN}{U_S(T)}\right) \tag{2}$$

$$T = \frac{-1}{k_b m} \tag{3}$$

where h, c, and N respectively represent Planck's constant, the speed of light, and total species population and m refers to the slope of the Boltzmann plot. Plotting the left hand side quantity for various lines of the same species against their upper energy levels (E_k) yields a Boltzmann plot; performing a line fit to the plot and obtaining the slope m allows for the calculation of temperature as $T = \frac{-1}{k_b m}$, independent of the y-intercept, and therefore the total species population N. The species concentrations were determined from this calculated temperature using the measured line intensities in conjunction with the calculated partition function, tabulated transition parameters, and the evaluated temperature.

An abundance of Si I emissions listed in Table 2, were identified in the spectra of both samples and used to calculate temperature for each measurement location. Because the Boltzmann method extracts the plasma temperature from the slope of a linear regression fit dependent on upper-level energies of the emission lines, a reliable temperature determination generally requires emission lines spanning a broad range of excitation energies.[53] In this study, due to the wider gate width employed in the LIBS measurements to improve SNR, we employed the selection criteria proposed by De Giacomo *et al.* for calculating temperature by excluding (i) resonant lines, (ii) lines with a transition probability less than $2 \times 10^6\ \mathrm{s}^{-2}$, (iii) ionic lines, and (iv) lines with NIST tabulated relative intensities >3000.[54] These selection criteria, along with demonstrating the validity of the McWhirter criterion, provide sufficient confidence of the LTE conditions and the validity of Boltzmann statistics to use CF-LIBS for elemental quantification. The Saha–Boltzmann approach is also known to be more accurate than the traditional Boltzmann method due to the broader range of energies from neutral and ionized species transitions,[55] but it was not feasible to use in this study as too few ionized lines were observed or easily resolved support a reliable fit. Fig. 12(a and b) show selected Boltzmann plot fits parameters, and uncertainty metrics for selected measurement locations on both samples.

Table 2 Neutral, non-resonant silicon lines utilized to calculate plasma temperature

λ (nm)	$g_k A_{ki}$ (s^{-1})	E_i (eV)	E_k (eV)
212.41	2.08×10^9	0.7810	6.6161
221.65	3.18×10^8	0.0277	5.6192
243.49	2.22×10^8	0.7810	5.8708
250.68	2.74×10^8	0.0096	4.9548
251.60	8.40×10^8	0.0277	4.9538
251.93	1.65×10^8	0.0096	4.9296
252.41	2.22×10^8	0.0096	4.9201
252.86	2.71×10^8	0.0277	4.9296
263.11	3.18×10^8	1.9087	6.6191
288.14	6.51×10^8	0.7810	5.0823
390.52	3.99×10^7	1.9087	5.0823

Using the calculated plasma temperatures, the electron density of the LPP at each measurement location of both samples was calculated from the Stark broadening of the Si I emission at 288.4 nm using eqn (4), where $\Delta\lambda$ is the measured

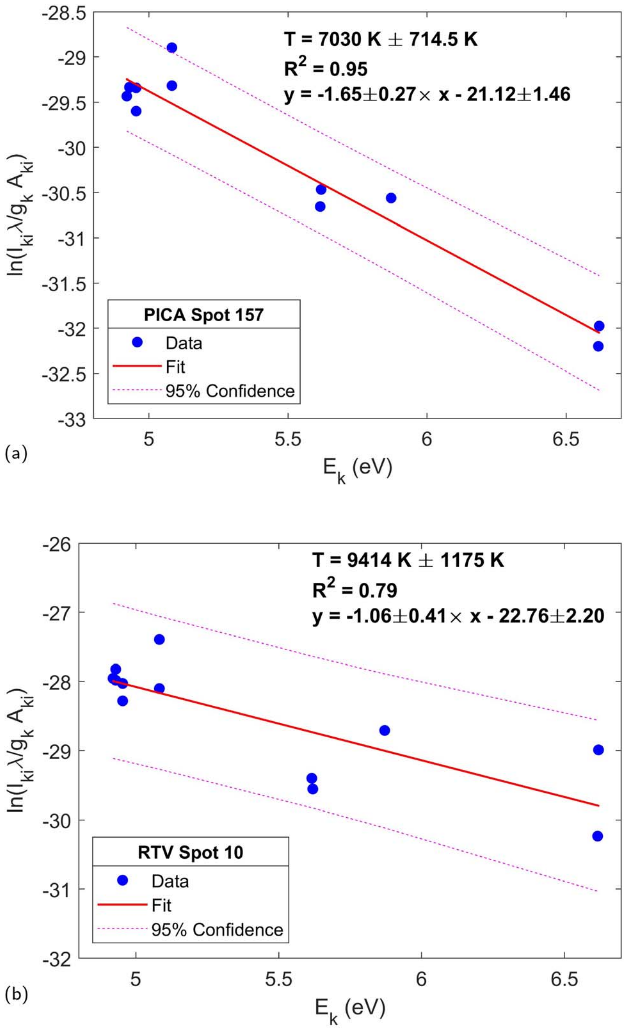

Fig. 12 Boltzmann temperature plot with fit error bounds, fit equation and uncertainties, and temperature value with error for (a) PICA measurement location 157 and (b) RTV measurement location 10.

Open Access Article. Published on 06 February 2026. Downloaded on 4/18/2026 5:39:06 PM.
This article is licensed under a Creative Commons Attribution 3.0 Unported Licence.

broadening of the line and w is the impact width parameter tabulated in Griem.[56]

$$n_e = \left(\frac{\Delta\lambda}{2w}\right) \times 10^{16}\left[\mathrm{cm}^{-3}\right] \tag{4}$$

Using the McWhirter criterion with the calculated temperatures and densities at each shot location, the LHS of eqn (1) ranged from $6.65 \times 10^{16} \pm 1.79 \times 10^{15}$ to 7.58×10^{16} cm^{-3} $\pm 1.16 \times 10^{16}$ for PICA and $6.65 \times 10^{16} \pm 3.19 \times 10^{15}$ to $6.94 \times 10^{16} \pm 1.25 \times 10^{15}$ cm^{-3} for the RTV shot locations. The RHS ranged from $2.15 \times 10^{16} \pm 1.08 \times 10^{15}$ to $2.48 \times 10^{16} \pm 1.02 \times 10^{16}$ cm^{-3} for PICA and $2.58 \times 10^{16} \pm 3.44 \times 10^{15}$ to $2.76 \times 10^{16} \pm 2.54 \times 10^{15}$ cm^{-3} for RTV. In this experiment, given that the calculated McWhirter criterion for all PICA and RTV locations is always lower than the computed electron density, the pLTE condition is validated for all data points. This is visually presented in Fig. 13(a and b) which shows the LHS and RHS quantity of the criterion calculated for each measurement location on both samples. Thus, the plasma temperatures at each measurement location calculated *via* the Boltzmann method with the Si I lines can be used to describe the LPP temperature for each respective location.

It should be noted that, in this study, a large gate width of 10 µs was selected primarily to discriminate against the continuum emission for minor and trace element detection. This is a standard practice[57–59] in traditional LIBS setups. Although the closure relation (*i.e.*, $\sum C_S = 1$) discussed in Section 5.2 has an effect on composition estimates for minor and trace elements due to error differences with major (abundant) elements, these errors related to insufficient signal-to-noise ratio are more pronounced.[60]

To address the issue related to the LTE assumption and sufficiently large gate for high SNR, De Giacomo *et al.*[54] proposed the following mitigation. The excitation temperature obtained from the Boltzmann plot can be treated as an average across time if the observed emissions are approximately constant during the selected interval of detection. Given the long integration forced by a 10 µs gate for sufficient SNR, this necessitates the following selection criteria:

(1) Emission lines involving the ground state were excluded to minimize resonance effects. From the original and revised manuscripts and all analyses, Si I at 220.8 nm and 251.41 nm were removed.[54]

(2) Transitions with spontaneous emission rates (A_{ki}) < 2×10^6 s^{-1} were removed such that all emission times are comparable to the associated time for transient plasma variations.[54,61]

(3) Due to deviations which can result from the Saha equation for ionic emissions related to recombination during expansion, only atomic (neutral) emissions were considered. This is inherent to the Boltzmann plot method.[54,61]

(4) All emission lines with tabulated relative intensities >3000 were excluded to filter out intensity values affected by noise and ensure sufficiently high SNR to ensure less significant effect on temperature calculations. Emissions with high intensity values are recommended to be excluded because they may be affected by broadening and saturation effects.[53,54]

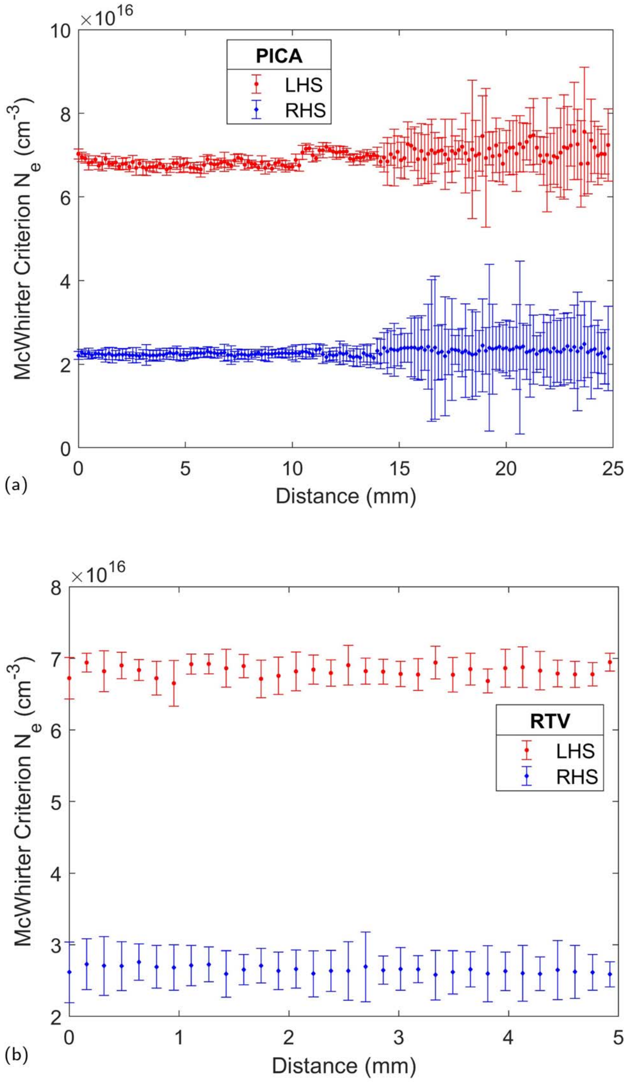

Fig. 13 Comparison of the LHS and RHS of the McWhirter criterion computed for each measurement location of (a) PICA and (b) RTV samples, visually demonstrating validity of eqn (1).

In addition to the pLTE conditions confirmed through the McWhirter criterion, these mitigation methods ensure that LTE conditions are met, and the Boltzmann method applied is valid.

5.2 CF-LIBS methodology

Assuming a LPP in partial local thermodynamic equilibrium that is optically thin, the intensity of an emitted line ($I_\lambda{}^{ki}$) is expressed by eqn (5),[24]

$$I_\lambda{}^{ki} = FC_S\frac{g_k A_{ki}}{U_S(T)}\exp\frac{-E_k}{k_b T} \tag{5}$$

using the degeneracy of the upper energy level k (g_k) and transition probability (A_{ki}) of the line, partition function of the elemental species U_S at temperature T, the upper energy level of the transition E_k, and the Boltzmann constant k_b. This equation must first be rearranged to find F, which is a normalization factor calculated assuming the closure relation where the sum of all species concentrations $\sum C_S = 1$,[24] to obtain eqn (6),

Open Access Article. Published on 06 February 2026. Downloaded on 4/18/2026 5:39:06 PM.
This article is licensed under a Creative Commons Attribution 3.0 Unported Licence.

$$\sum_{S} C_{S} = \frac{1}{F}\sum_{S}\frac{I_{\lambda}^{ki} U_{S}(T)}{g_k A_{ki}}\exp\frac{E_k}{k_b T} = 1 \tag{6}$$

where the partition function is calculated using eqn (7) from data in the NIST ASD lines tool at temperatures calculated through the Boltzmann method:

$$U_{S}(T) = \sum_{k} g_k \exp\frac{-E_k}{k_b T} \tag{7}$$

Determining F from eqn (6) using the parameters for every identified emission in the spectrum then allows the calculation of the relative concentration of each individual species from eqn (5). At each shot location, the temperature determined from the Si I lines in Section 5.1 was used for the calculation of the partition function of each species and in eqn (5). This method is valid due to the fulfillment of the criterion for pLTE demonstrated in the previous section. Thus, a Boltzmann plot for each species was not required, and the parameters from the emission lines in Table 1 were used with eqn (5) to determine each relative species concentration. This method is demonstrated in literature in several prior studies, also referred to as one-line CF-LIBS.[62–64] Cavalcanti *et al.*[65] specifically implements this methodology and cites the McWhirter criterion[52] to justify the assumption of a single temperature and the use of eqn (5) to determine species concentrations. The associated line parameters necessary for this calculation (*e.g.*, upper level energy, transition probability) are found using the NIST database. This analytical process was repeated for the PICA and RTV samples separately at each location along the depth profile due to variations in sample composition.

Where applicable, the contributions of different ionization states (*e.g.*, Si I and Si II) of an element are added together to determine a total relative concentration for the individual species ($C_{\mathrm{Si}}^{\mathrm{TOT}} = C_{\mathrm{Si}}^{(\mathrm{I})} + C_{\mathrm{Si}}^{(\mathrm{II})}$).[24] The validity of this approach relies on the widely adopted, first-order approximation for CF-LIBS that the observed emission spectrum captures the complete sample composition.[66] It should also be noted that, while resonance lines are generally prone to self-absorption effects (*e.g.*, Na I and K I in Table 1), this issue can become negligible at sufficiently low pressures, and is thus not accounted for in the CF-LIBS algorithm of this study due to the vacuum conditions under which measurements were taken.[67]

5.3 Cross-section profiles of PICA and RTV

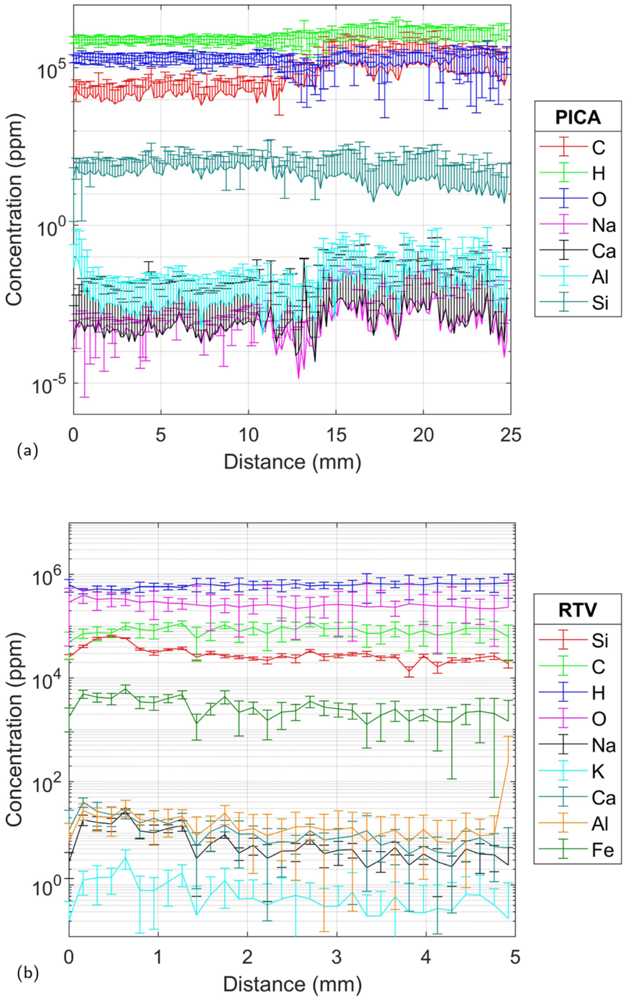

Fig. 14 Species concentrations across linear cross sections of samples of (a) PICA and (b) RTV silicone investigated in this experiment.

Fig. 14(a) and (b) show the concentrations in parts-per-million (ppm) (C_s) of each main species listed in Table 1 calculated using eqn (5) as a function of cross-sectional distance through each sample. Error bars are determined using shot-to-shot standard deviation of peak area at each location, propagated according to basic statistical error formulae. As expected, PICA is mainly composed of C, H, and O with respective concentration ranges of $6.2 \times 10^3 \pm 7.7 \times 10^2$–$2.0 \times 10^5 \pm 1.3 \times 10^5$ ppm (C), $5.5 \times 10^5 \pm 9.1 \times 10^4$–$9.1 \times 10^5 \pm 3.2 \times 10^5$ ppm (H), and $7.0 \times 10^4 \pm 3.0 \times 10^4$–$3.2 \times 10^5 \pm 3.8 \times 10^4$ ppm (O) across the sample. The calculations reveal an interesting result in the unexpectedly high concentration of Si ranging from 4.21 ± 2.32 to 230 ± 46.0 ppm across the sample. The Si concentration presents at a higher concentration on the order of 10^2 ppm from 0–12 mm into the cross section, and then drops to 10^1 ppm across the remainder of the profile. The inverse of this trend is seen in the C concentration, which rises from $\sim 10^4$ to 10^5 ppm after 12 mm. We attribute this trend to the use of a proprietary waterproof coating used on the PICA tiles prior to assembly of the heatshield. The coating likely penetrates into the tile through the layers of carbon fibers, causing the higher Si concentrations observed in the first 12 mm of the sample. The root cause of the presence of Si in the uncoated PICA is still unknown and will be the subject of further investigation into these materials. The remaining identified elemental contaminants are Ca, Al, and Na, present in trace concentrations of $4 \times 10^{-5} \pm 6 \times 10^{-4}$–$0.01 \pm 0.05$ ppm (Ca), $6.5 \times 10^{-3} \pm 6.0 \times 10^{-4}$–$0.91 \pm 0.14$ ppm (Al), and $1 \times 10^{-5} \pm 9 \times 10^{-5}$–$0.010 \pm 0.019$ ppm. The larger error bars in the calculated quantities of these three elements are a direct result of higher shot-to-shot variation in the emission line intensity of these minor analytes across the sample. These results reflect previous reporting of

Open Access Article. Published on 06 February 2026. Downloaded on 4/18/2026 5:39:06 PM.
This article is licensed under a Creative Commons Attribution 3.0 Unported Licence.

lower accuracy in trace level analyte quantification using CF-LIBS, particularly when the analyte concentration is below the single part-per-million level.[31–33] Although the consistent appearance of the emissions of these elements in the recorded spectra provides confidence of their presence across the sample, the larger the uncertainty of their calculated concentration is critical to note when performing quantitative analysis. If truly high fidelity quantification is required, these results should be compared to concentrations determined from robust mass spectrometry methods as a validation.

The RTV linear profile composition depicted in Fig. 14(b) indicates the sample is composed primarily of H, O, C, and Si. This is expected as the molecular structure of silicone consists of a siloxane backbone (Si–O–Si–O) and attached organic groups such as methyl (CH_3). The concentrations of the 4 major elemental constituents are relatively constant across the measurement, presenting average values of $6.2 \times 10^5 \pm 1.8 \times 10^5$ ppm (H), $2.7 \times 10^5 \pm 2.2 \times 10^4$ ppm (O), $8.4 \times 10^4 \pm 3.2 \times 10^4$ ppm (C), and $3.0 \times 10^4 \pm 2.6 \times 10^3$ ppm (Si). The variant of RTV silicone used in this study contains iron oxide as an additive for high temperature applications. It is assumed that iron oxide is mixed during manufacturing such that it is homogeneous in the final material. A pronounced presence of Fe, averaging $2.7 \times 10^3 \pm 5.9 \times 10^2$ ppm, was measured, consistent with the radiant emission of Fe observed in the shock layer during reentry. While Fe is not an intrinsic contaminant of the base material, it is designated as a such due to its anomalous radiative emission in the context of this experiment. Multiple alkali and alkaline earth (Ca, Na, K) metals as well as Al are present through the sample. Al and Ca appear with average concentrations of 21.0 ± 13.0 and 11.0 ± 6.0 ppm, respectively. Na presents with an average concentration of 7.1 ± 2.4 ppm, while K is seen at the lowest average concentration of 0.71 ± 0.7 ppm. The average concentration of Na calculated in the RTV sample is 2 orders of magnitude greater than that in the PICA, helping to explain the persistent radiance of the Na doublet reflected in Fig. 2. Similarly, Ca is found in the RTV at concentrations 3 orders of magnitude higher than those of PICA. Based on these observations, we posit that much of the apparent radiance of these metallic species observed in the flight data originates from shock-heated air interacting with the RTV silicone, with minor contributions from the release of trace metal impurities during pyrolysis and ablation of the PICA matrix. These measurements reflect the utility of the CF-LIBS method and the value in performing benchtop analyses of TPS material composition. A full understanding of the TPS sample chemistry elucidates the causes of the unexpected spectral emissions seen in the flight data, helping to better correlate the effects of these impurities on shock layer thermochemistry. A comprehensive tabulation of the measured elemental concentrations at each location for both samples is provided in the SI file for this manuscript. To further investigate the physical phenomena corresponding to the release of these species during flight, we examine the fundamental chemical properties of these elements as well as the aerodynamics of the vehicle.

6 Discussion on aerothermodynamic phenomena and effects of metallic contaminants in the shock layer

The Varda capsule forebody is comprised of three tiled sections: one nose tile, followed by concentric rows of midsection and shoulder tiles. Fig. 15(a) shows the forebody of W-2. The middle section tile gap in this image was directly in line with the collimating lens of OSPREE placed behind the optical window above the shoulder section. Thus, it is highly likely that ablated material from the PICA tiles and the RTV between the tiles was observed in the recorded shock layer emissions. The thermal decomposition of the PICA tiles, through processes such as pyrolysis and ablation, introduce C, H, O, and trace metallic species into the shock layer. These species in turn undergo

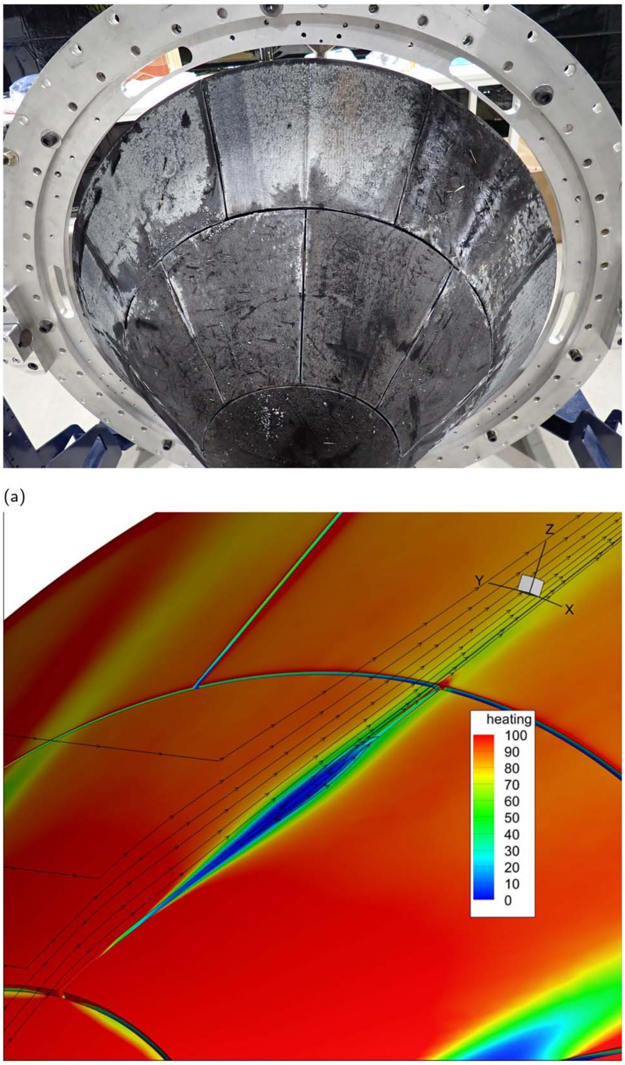

Fig. 15 (a) Picture of the W-2 capsule forebody showing charred PICA tiles, structure, and tile gaps. (b) CFD simulation of flow streamlines through tile gaps which expand into cavities, releasing RTV decomposition products into the shock layer.

Open Access Article. Published on 06 February 2026. Downloaded on 4/18/2026 5:39:06 PM.
This article is licensed under a Creative Commons Attribution 3.0 Unported Licence.

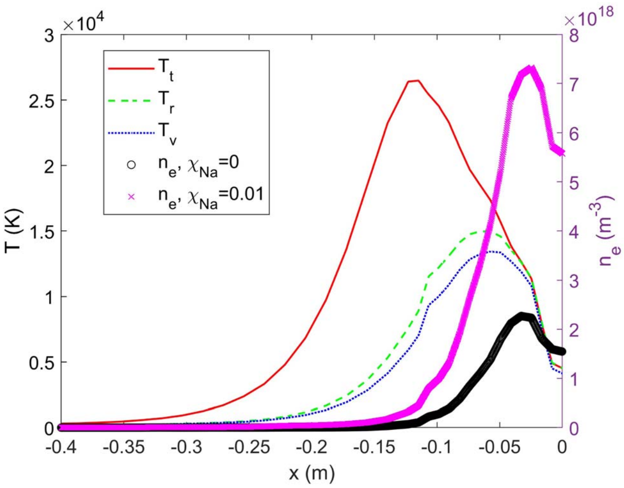

Fig. 16 Fluid dynamics simulation results of the NASA RAM-C II vehicle along an antenna's line of sight showing shock layer translational (T_t), rotational (T_r), and vibrational (T_v) temperatures as well as electron density (n_e) with (magenta) and without (black) the addition of a small amount of sodium to the shock layer.

chemical reactions with shock heated air molecules, as well as collisional and radiative excitation and ionization. These processes contribute to the carbon molecular emission signatures seen in Fig. 2(a), in addition to some of the early Ca, Fe, and Na atomic emission lines. Since the nose tile of the capsule experiences the highest heat flux (300 W cm^{-2}) at the stagnation point, it is expected to contribute to most of the early shock layer trace species emissions.

In addition to heatshield decomposition from thermal loading, aerodynamic effects in gaps between the forebody tiles contribute to the presence of metallic species emissions in the spectral data. The high enthalpy flow penetrates the tile gaps, which consequently expand into cavities, thus exposing the RTV to high heat fluxes. This decomposes the first few mm of the RTV and introduces gaseous RTV constituents (Si, O, C, H, Fe) into the shock layer. The higher concentration of minor metals (Ca) in the RTV compared to the PICA likely contributes to the initial rise in Ca radiance seen in Fig. 2(b), as the erosion in the tile gap would introduce these minor metals into the shock layer. A coarse mesh computational fluid dynamics (CFD) simulation of this cavity flow is shown in Fig. 15(b). The simulation indicates that the cavities initially entrain flow into themselves, resulting in higher heating at the leading edge of the gaps. Subsequently, the mid-row cavities establish a vortex towards the center of the cavity that ejects flow from the cavity back into the shock layer. These vortices help reradiate heat from the vehicle back into the shock layer. Thus, the RTV at the leading edge of the cavity is expected to decompose and erode into the shock layer. Since the collimating lens of OSPREE was directly upstream and in line from a midsection tile gap, we conclude that the recorded Fe emissions and the persistent presence of Na and Ca in the data are a direct result of the flow-induced decomposition of the RTV in this midsection tile gap. Proper understanding of how aerothermodynamic phenomena and gas–surface interactions drive the radiance of metallic TPS impurities in the shock layer is key to assessing TPS performance and optimizing reentry spacecraft design. An improved understanding of the chemical makeup of common TPS materials can aid in identifying the sources of metallic contaminants during manufacturing to reduce or eliminate them from the material entirely. Subsequently, using TPS materials with less of these contaminants in spacecraft design would yield overall lower radiative heating, reducing the total heat load experienced by the vehicle. This would enable a reduced total mass of TPS needed to ensure vehicle survivability, boosting both available payload mass and aerodynamic performance as a result.

Furthermore, knowing the amounts of trace contaminants in the TPS, especially alkali metals, can enable better fluid dynamics modeling predictions of the flowfield chemistry and analysis of other physical effects caused by the presence of such species. Fig. 16 shows results from the fluid dynamics simulation of a commonly simulated historical test vehicle (NASA RAM C-II)[68] where a small mole fraction of Na was added to the simulation. The electron density along a line of sight corresponding to the location of a receiving antenna is shown. The addition of 0.01 mole fraction of Na increases the maximum electron density by a factor of 3.2, largely due to the impact ionization reaction discussed in Section 2. The plasma frequency (ω_{pe}), given by

$$\omega_{pe} = \sqrt{\frac{n_e e^2}{m_e \varepsilon_0}} \tag{8}$$

is dependent on the electron density (n_e) as well as the constants of electron charge (e), electron mass (m_e), and permittivity (ε_0). An increase in the maximum electron density from 2.27 × 10^{18} m^{-3} to 7.32 × 10^{18} m^{-3} increases the plasma cutoff frequency from 13.5 GHz to 24.3 GHz, worsening incident signal attenuation or contributing to complete RF blackout depending on the incident frequency. While this analysis has been greatly simplified for the purpose of demonstrating fundamental principles, it underscores an important conclusion: knowing precise quantities of these contaminant species can help yield more accurate analysis and models of their effects on vehicle performance.

7 Conclusions

We report the chemical characterization of PICA and RTV using CF-LIBS and the identification of several metallic contaminants such as Si, Na, Ca, K, Al, and Fe in these TPS materials. Cross-section profiles of each material using CF-LIBS are presented, characterizing depth-dependent concentration of the varying metallic elements. It is determined that PICA contains trace amounts (0.001–1 ppm) of Na, Ca, and Al, in addition to Si on the order of 10^2 ppm due to the application of a waterproof coating. The RTV silicone is characterized by higher levels of alkali/alkaline earth metals (10^1 ppm), along with a large amount of Fe (10^3 ppm) as an additive for high temperature applications. Pyrolysis and ablation of PICA during reentry, as

Open Access Article. Published on 06 February 2026. Downloaded on 4/18/2026 5:39:06 PM. This article is licensed under a Creative Commons Attribution 3.0 Unported Licence.

well as decomposition and erosion of the RTV silicone between tile gaps due to the high enthalpy cavity flow, introduce these metallic elements into the shock layer. The subsequent excitation and radiation of these metals explains the strong spectral radiance of Na and Fe observed in shock layer OES measurements of the Varda W-2 reentry capsule. Quantification of these contaminants will enable higher fidelity modeling of the TPS-shock layer reaction chemistry to account for enhanced radiative heating and electron generation, contributing to the development of higher-performing future reentry spacecraft.

Conflicts of interest

There are no conflicts to declare.

Data availability

Data are available upon request from the authors.

Supplementary information (SI) is available. See DOI: https://doi.org/10.1039/d5ja00374a.

Acknowledgements

Distribution unlimited; approved for public release. AFRL Public Affairs Release #AFRL-2025-4812. This work was funded by the Air Force Office of Scientific Research (AFOSR), Lab Task RVCOR005, through the High-Speed Aerodynamics Portfolio (Dr Amanda Chou). The W-2 flight test was funded under SPACEWERX STRATFI contract FA-9453-23-C-A035. Development of OSPREE was funded through contract FA-9453-18-D-0042. The authors acknowledge funding from the Universities Space Research Association and the AFRL Scholars Program. The authors would like to thank their colleagues at NASA Ames Research Center, Thermal Protection Materials and Aerothermodynamics branches, for their thoughtful discussions on these results which contributed to the analysis. The views expressed are those of the authors and do not necessarily reflect the official policy or position of the Department of the Air Force, the Department of Defense, or the U.S. government.

References

1 C. Park, *Nonequilibrium Hypersonic Aerothermodynamics*, Wiley, 1990.

2 J. J. Bertin and R. M. Cummings, *Annu. Rev. Fluid. Mech.*, 2006, **38**, 129–157.

3 B. K. Bessire, S. A. Lahankar and T. K. Minton, *ACS Appl. Mater. Interfaces*, 2015, **7**, 1383–1395.

4 B. K. Bessire and T. K. Minton, *ACS Appl. Mater. Interfaces*, 2017, **9**, 21422–21437.

5 M. W. Winter, *19th AIAA International Space Planes and Hypersonic Systems and Technologies Conference*, Atlanta, GA, 2014.

6 M. Winter, B. Butler, P. M. Danehy, S. Splinter, Z. Diao, F. Panerai, A. Martin and S. Bailey, *46th AIAA Thermophysics Conference*, 2016, p. 3233.

7 A. P. Rao, J. D. Crespo, P. Valentini, J. B. Taylor, V. J. Murray, E. I. Vaughan, R. Alviani and M. Kulakhmetov, *J. Spacecr. Rockets*, 2025, **62**, 1486–1495.

8 M. F. Kulakhmetov, R. Alviani, A. Rao, V. Murray, J. B. Taylor, J. Seik and E. Vaughan, *AIAA Aviation Forum and Ascend 2024*, 2024, p. 4560.

9 M. Kulakhmetov, M. Gallis and A. Alexeenko, *J. Chem. Phys.*, 2016, **144**, 1–15.

10 D. W. Hahn and N. Omenetto, *Appl. Spectrosc.*, 2012, **66**, 347–419.

11 S. K. H. Shah, J. Iqbal, P. Ahmad, M. U. Khandaker, S. Haq and M. Naeem, *Radiat. Phys. Chem.*, 2020, **170**(33), 108666.

12 D. A. Cremers and L. J. Radziemski, *Handbook of Laser-Induced Breakdown Spectroscopy*, John Wiley & Sons, 2013.

13 R. S. Harmon, J. Remus, N. J. McMillan, C. McManus, L. Collins, J. L. Gottfried Jr, F. C. DeLucia and A. W. Miziolek, *Appl. Geochem.*, 2009, **24**, 1125–1141.

14 R. Anderson, T. Gabriel, O. Forni, J. Manrique, P. Gasda, D. Vogt, A. Ollila *et al.*, *54th Lunar and Planetary Science Conference 2023*, 2023, p. 2182.

15 K. C. Hartig, I. Ghebregziabher and I. Jovanovic, *Sci. Rep.*, 2017, **7**, 43852.

16 M. B. Shattan, M. Gragston, Z. Zhang, I. J. D. Auxier, K. G. McIntosh and C. G. Parigger, *Appl. Spectrosc.*, 2019, **73**, 591–600.

17 A. P. Rao, P. R. Jenkins, J. D. Auxier, M. B. Shattan and A. K. Patnaik, *Appl. Opt.*, 2022, **61**, D30–D38.

18 P. E. Anderson, J. I. Braun, J. I. Borrero Negrón, K. C. Hartig and A. P. Rao, *Appl. Opt.*, 2025, **64**, D122–D132.

19 Z. B. Kitzhaber, D. Orea, J. McFarlane, B. T. Manard and H. B. Andrews, *ACS Omega*, 2025, **10**(33), 37889–37897.

20 R. Noll, C. Fricke-Begemann, S. Connemann, C. Meinhardt and V. Sturm, *J. Anal. At. Spectrom.*, 2018, **33**, 945–956.

21 M. Dell'Aglio, R. Gaudiuso, G. S. Senesi, A. De Giacomo, C. Zaccone, T. M. Miano and O. De Pascale, *J. Environ. Monit.*, 2011, **13**, 1422–1426.

22 Y. Zhang, T. Zhang and H. Li, *Spectrochim. Acta, Part B*, 2021, **181**, 106218.

23 G. Radhakrishnan, P. Adams and L. Bernstein, *J. Appl. Phys.*, 2023, **134**(1), 013303.

24 A. Ciucci, M. Corsi, V. Palleschi, S. Rastelli, A. Salvetti and E. Tognoni, *Appl. Spectrosc.*, 1999, **53**, 960–964.

25 N. Zhang, T. Ou, M. Wang, Z. Lin, C. Lv, Y. Qin, J. Li, H. Yang, N. Zhao and Q. Zhang, *Front. Phys.*, 2022, **10**, 887171.

26 J. Yang, X. Li, J. Xu and X. Ma, *Appl. Spectrosc.*, 2018, **72**, 129–140.

27 R. Pamu, S. A. Davari, D. Darbar, E. C. Self, J. Nanda and D. Mukherjee, *ACS Appl. Energy Mater.*, 2021, **4**, 7259–7267.

28 L. C. L. Borduchi, D. M. B. P. Milori, M. C. Meyer and P. R. Villas-Boas, *Spectrochim. Acta, Part B*, 2022, **198**, 106561.

29 E. Tognoni, G. Cristoforetti, S. Legnaioli and V. Palleschi, *Spectrochim. Acta, Part B*, 2010, **65**, 1–14.

30 J. Hermann, C. Gerhard, M. Burger, V. Craciun and F. Pelascini, *Spectrochim. Acta, Part B*, 2023, **200**, 106595.

31 P. R. Villas-Boas and L. C. L. Borduchi, *Spectrochim. Acta, Part B*, 2023, **205**, 106690.

This journal is © The Royal Society of Chemistry 2026

Open Access Article. Published on 06 February 2026. Downloaded on 4/18/2026 5:39:06 PM.
This article is licensed under a Creative Commons Attribution 3.0 Unported Licence.

32 S. Pandhija, N. Rai, A. K. Rai and S. N. Thakur, *Appl. Phys. B*, 2010, **98**, 231–241.
33 M. Shah, A. Pulhani, G. Gupta and B. Suri, *Appl. Opt.*, 2012, **51**, 4612–4621.
34 A. P. Rao, J. D. Crespo, P. Valentini, J. B. Taylor, V. J. Murray, E. I. Vaughan, R. Alviani and M. Kulakhmetov, *J. Spacecr. Rockets*, 2025, 1–15.
35 K.-P. Schneider and C. Park, *Phys. Fluids*, 1975, **18**, 969–981.
36 M. H. Bortner, *The Chemical Kinetics of Sodium in Re-entry*, General electric technical report, 1964.
37 M. Lennon, K. Bell, H. Gilbody, J. Hughes, A. Kingston, M. Murray and F. Smith, *J. Phys. Chem. Ref. Data*, 1988, **17**, 1285–1363.
38 M. Jung, H. Kihara, K.-i. Abe and Y. Takahashi, *47th AIAA Fluid Dynamics Conference*, 2017, p. 3308.
39 Y. Ralchenko, *Mem. Soc. Astron. Ital.*, 2005, **8**, 96.
40 J. Zhong and D. A. Levin, *J. Spacecr. Rockets*, 2010, **47**, 757–764.
41 C. O. Johnston, *AIAA Aviation 2022 Forum*, 2022, p. 3799.
42 S. W. Lewis, R. G. Morgan, T. J. McIntyre, C. R. Alba and R. B. Greendyke, *J. Spacecr. Rockets*, 2016, **53**, 887–899.
43 S. W. Lewis, C. M. James, R. G. Morgan, T. J. McIntyre, C. R. Alba and R. B. Greendyke, *J. Thermophys. Heat Transfer*, 2017, **31**, 193–204.
44 H. Tran, C. Johnson, D. Rasky, F. Hui, M.-T. Hsu and Y. Chen, *31st Thermophysics Conference*, 1996, p. 1911.
45 M. Gasch, K. Skokova, M. Stackpoole, E. Venkatapathy, D. Ellerby, F. Milos, K. Peterson, D. Prabhu, G. Gonzales, S. Violette *et al.*, *Development of Domestic Lyocell Based Phenolic Impregnated Carbon Ablator (PICA-D) for Future NASA Missions*, National aeronautics and space administration technical report, 2019.
46 M. M. Stackpoole, M. J. Gasch, E. Venkatapathy and S. Violette, *National Space and Missile Materials Symposium (NSMMS)*, 2019.
47 I. Karnadi, M. Pardede, I. Tanra, R. Hedwig, A. M. Marpaung, Z. S. Lie, E. Jobiliong, D. Kwaria, M. M. Suliyanti, M. Ramli, K. Lahna, T. J. Lie, H. Suyanto, K. H. Kurniawan and K. Kagawa, *Sci. Rep.*, 2020, **10**, 13278.
48 J. A. J. Effenberger and J. R. Scott, *Sensors*, 2010, **10**, 4907–4925.
49 Z. Q. Hao, L. Liu, M. Shen, X. Y. Yang, K. H. Li, L. B. Guo, X. Y. Li, Y. F. Lu and X. Y. Zeng, *Opt. Express*, 2016, **24**, 26521–26528.
50 N. Karim, M. P. Polek, A. M. Casella, D. J. Senor, S. S. Harilal and E. J. Kautz, *Spectrochim. Acta, Part B*, 2025, **223**, 107081.
51 M. Dell'Aglio, M. López-Claros, J. Laserna, S. Longo and A. De Giacomo, *Spectrochim. Acta, Part B*, 2018, **147**, 87–92.
52 T. Fujimoto and R. McWhirter, *Phys. Rev. A*, 1990, **42**, 6588.
53 B. Bousquet, V. Gardette, V. M. Ros, R. Gaudiuso, M. Dell'Aglio and A. De Giacomo, *Spectrochim. Acta, Part B*, 2023, **204**, 106686.
54 A. De Giacomo, M. Dell'Aglio, O. De Pascale, S. Longo and M. Capitelli, *Spectrochim. Acta, Part B*, 2007, **62**, 1606–1611.
55 T. Völker and I. B. Gornushkin, *J. Anal. At. Spectrom.*, 2022, **37**, 1972–1974.
56 H. Griem, *Spectral Line Broadening by Plasmas*, Elsevier, 2012.
57 M. Sabsabi and P. Cielo, *Appl. Spectrosc.*, 1995, **49**, 499–507.
58 E. Tognoni, V. Palleschi, M. Corsi and G. Cristoforetti, *Spectrochim. Acta, Part B*, 2002, **57**, 1115–1130.
59 C. Aragon, J. A. Aguilera and F. Penalba, *Appl. Spectrosc.*, 1999, **53**, 1259–1267.
60 J. Hermann, *Laser Induced Breakdown Spectroscopy (LIBS) Concepts, Instrumentation, Data Analysis and Applications*, 2023, vol. 1, pp. 89–121.
61 A. De Giacomo, *Spectrochim. Acta, Part B*, 2003, **58**, 71–83.
62 G. H. Cavalcanti, D. N. Stratis and C. Parigger, *Appl. Opt.*, 2012, **51**, 264–271.
63 Y. Fu, J. Liu, X. Li and Y. Zhang, *Appl. Spectrosc.*, 2014, **68**, 201–209.
64 M. Fahad, W. A. Farooq, A. Qayyum, S. A. Buzdar and A. Q. Malik, *AIP Adv.*, 2019, **9**, 095127.
65 G. Cavalcanti, D. Teixeira, S. Legnaioli, G. Lorenzetti, L. Pardini and V. Palleschi, *Spectrochim. Acta, Part B*, 2013, **87**, 51–56.
66 F. Poggialini, B. Campanella, B. Cocciaro, G. Lorenzetti, V. Palleschi and S. Legnaioli, *J. Anal. At. Spectrom.*, 2023, **38**, 1751–1771.
67 F. Rezaei, G. Cristoforetti, E. Tognoni, S. Legnaioli, V. Palleschi and A. Safi, *Spectrochim. Acta, Part B*, 2020, **169**, 105878.
68 W. L. Jones and A. E. Cross, *Electrostatic-probe Measurements of Plasma Parameters for Two Reentry Flight Experiments at 25000 Feet Per Second*, National Aeronautics and Space Administration, 1972, vol. 6617.